Electronic Supplementary Material (ESI) for Materials Horizons.

SUPPLEMENTARY INFORMATION FOR

Quantification of Ion Migration in $CH_3NH_3PbI_3$ Perovskite Solar Cells by Transient Capacitance Measurements

Moritz H. Futscher[1], Ju Min Lee[1], Lucie McGovern[1], Loreta A. Muscarella[1], Tianyi Wang[1], Muhammad Irfan Haider[2], Azhar Fakharuddin[2], Lukas Schmidt-Mende[2] and Bruno Ehrler[1]*

1. Center for Nanophotonics, AMOLF, Science Park 104,

   1098 XG Amsterdam, The Netherlands

2. Department of Physics, University of Konstanz, Universitätsstraße 10,

   78457 Konstanz, Germany

Corresponding Author

* ehrler@amolf.nl

S1 EFFECT OF CONTACT LAYERS

By measuring the current-voltage characteristic at different scan rates, a distinction can be made between capacitive and non-capacitive hysteresis.[1] Figure S1 illustrates the effect of capacitive hysteresis in perovskite solar cells using TiO_2 as an electron transport material. This effect is attributed to the accumulation of both ionic and electronic charges at the TiO_2/perovskite interface in a highly reversible manner resulting in a double-layer structure.[1] This effect is not observed in the inverted structure using NiO_x.

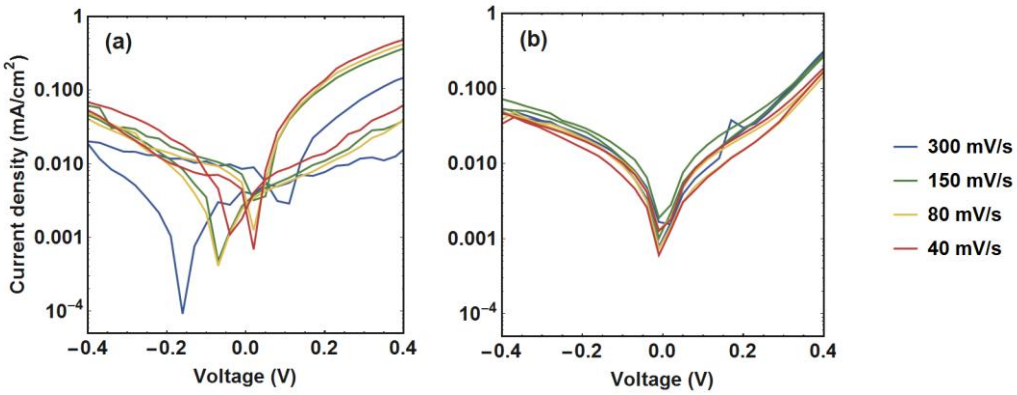

Figure S1. Dark current-voltage characteristics of diodes based on **(a)** TiO_2/$MAPbI_3$/spiro-OMeTAD and **(b)** NiO_x/$MAPbI_3$/C_{60} illustrating different hysteretic effects as a function of the scan rate.

Figure S2 shows the capacitance versus frequency at different temperatures for the inverted and the regular perovskite solar cell structure. At the temperature range between 180 and 300 K no phase transition of the $MAPbI_3$ layer is to be expected. However, the regular devices structure shows a strong change in the high-frequency region at these temperatures, indicating dielectric contributions of contact layers play an important role. For the measurement of transient ion-drift, such interfacial effects shall be minimized.

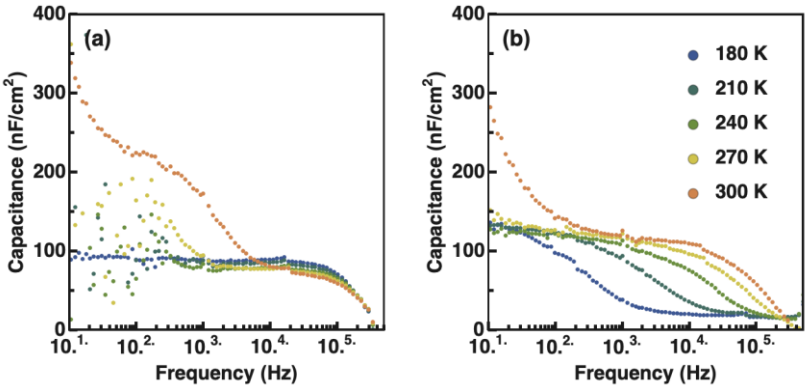

Figure S2. Impedance spectroscopy measured at different temperatures in the dark at 0 V with an AC perturbation of 20 mV of **(a)** an inverted (NiO_x/$MAPbI_3$/C_{60}) and **(b)** a regular (TiO_2/C_{60}/$MAPbI_3$/spiro-OMeTAD) and perovskite solar cell.

S2 DARK AND LIGHT CURRENT-VOLTAGE CHARACTERISTICS

Inverted perovskite solar cells have been shown to have only little hysteresis when illuminated,[2–5] but hysteresis may still be present in the dark. Figure S3 shows the current-voltage characteristic of an inverted perovskite solar cell measured with a scan rate of 300 mV/second under 1-Sun from a solar simulator (Oriel 92250A) using a Keithley 2636A source-measure unit after 15 minutes light soaking. During this measurement, the sample was masked and placed in nitrogen inside an air-tight sample holder. Figure S4 shows current-voltage characteristics of an inverted perovskite solar cell in the dark, measured between 180 and 330 K. We note that there is a significant difference between the current-voltage hysteresis measured in the dark and under illumination. This difference may be caused by photo-induced ion migration, which shifts the hysteretic response to different time scales. In fact, it has been shown that the activation energy for ion migration is reduced by illumination.[6,7] When the perovskite solar cell is cooled, the current-voltage hysteresis is reduced and almost vanishes at 180 K.

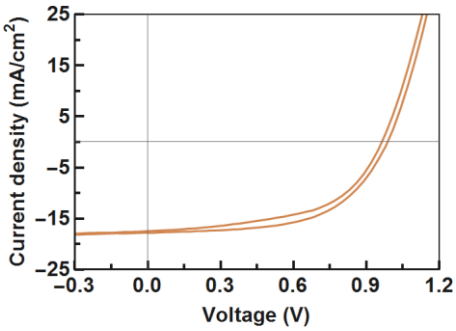

Figure S3. Current-voltage characteristics of an inverted perovskite solar cell (NiO_x/$MAPbI_3$/C_{60}) measured at 1-Sun at room temperature.

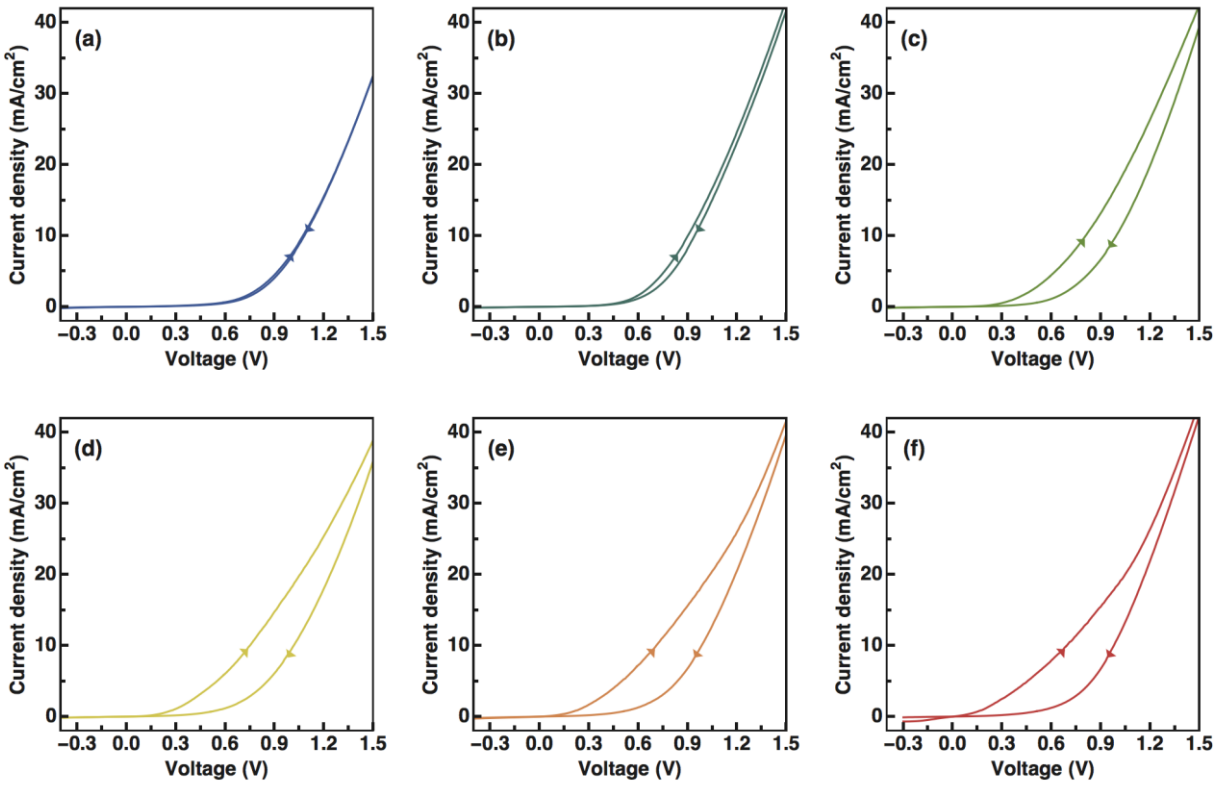

Figure S4. Temperature dependent current-voltage hysteresis measured in the dark at **(a)** 180 K, **(b)** 210 K, **(c)** 240 K, **(d)** 270 K, **(e)** 300 K, and **(f)** 330 K.

S3 MOTT-SCHOTTKY CHARACTERISTICS

Figure S5 shows the capacitance as a function of voltage measured at 10 kHz, where the measured capacitance corresponds to the geometric capacitance and the series resistance can be neglected (see Figure 1c). We observe a plateau at low voltage, which indicates full

depletion under short-circuit conditions. In such a case of full depletion, the geometrical capacitance can be related to the perovskite permittivity. Assuming a parallel plate capacitor with the thickness of the perovskite layer, we obtain a permittivity of 15.3 for the perovskite layer, averaged over the measured temperatures, somewhat lower than the calculated value of 24.1 from electronic structure calculation in the absence of molecular reorientations.[8]

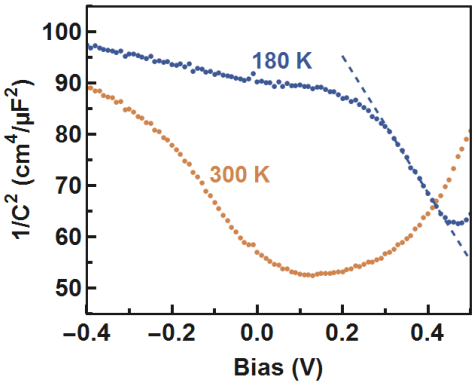

Figure S5. Mott-Schottky characteristics of an inverted perovskite solar cell (NiO_x/$MAPbI_3$/C_{60}) measured at 300 and 180 K in the dark with an AC perturbation of 10 mV at 10 kHz.

When a voltage V is applied in forward direction, the depletion capacitance C_D is increased. This increase in capacitance is correlated to a decrease in depletion-layer width. The depletion capacitance as a function of applied voltage can be approximated by the Mott-Schottky relation as

$$C_D = \sqrt{\frac{q\ \varepsilon_0\ \varepsilon\ N}{2\ (V_B - V)}}$$

where q is the elementary charge, ε_0 the vacuum permittivity, ε the perovskite permittivity, N the doping density, and V_B the built-in potential.[9] From the $C^{-2}(V)$ plot we obtain a built-in potential of 0.92 V and a doping density of 7.0 x 10^{16} cm^{-3}. The slope of the Mott-Schottky plot furthermore suggests a p-type $MAPbI_3$ layer. Theoretical calculations predict that the p-type doping of $MAPbI_3$ originates from negatively charged Pb^{2+} and MA^+ vacancies, where

positively charged I^- vacancies might result in n-type doping.[10] Note that the Mott-Schottky analysis is only meaningful when the depletion capacitance can be clearly identified.[11] Since the ionic capacitance contribution dominates the depletion capacitance at high temperatures, we performed the Mott-Schottky analysis at 180 K.

For the calculation of the concentration of mobile ions, a constant doping density of 1×10^{17} cm^{-3} is assumed for all devices. Since our obtained doping concentration at 180 K is close to typical vales at room temperature (1×10^{17} cm^{-3}),[11] we believe that the measured temperature window lies within the extrinsic region in which the doping density is reasonably constant.

S4 ION REDISTRIBUTION

Figure S6 shows the amplitude of the capacitance transient as a function of filling pulse duration. Since the amplitude has reached its maximum at 1 second filling pulse duration, we assume that a uniform ion distribution is reached after applying a filling pule of 1 second.

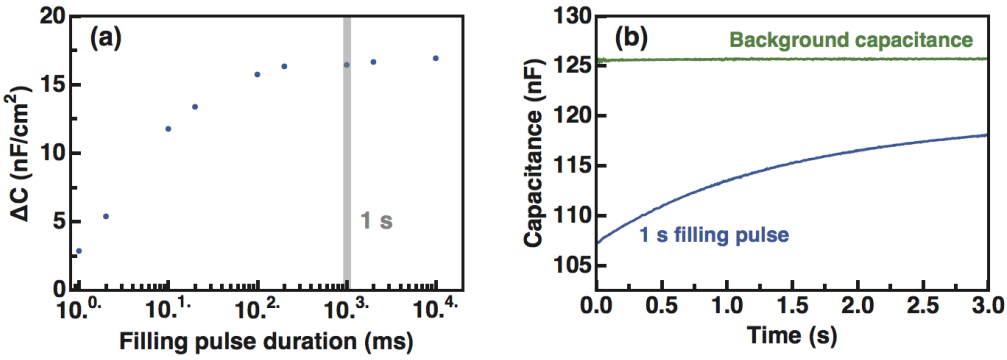

Figure S6. (a) Amplitude of the capacitance transient when applying a voltage of 0.4 V as a function of filling pulse duration. The grey line indicates the filling pulse duration used for the transient ion-drift measurements. **(b)** Background capacitance and capacitance transient after applying a filling pulse of 0.4 V for 1 second at 300 K. The capacitance transient was measured after the background capacitance had reached a steady state.

S5 TRANSIENT ION-DRIFT

Transient ion-drift is a powerful method to quantify mobile ions in perovskite materials with very high accuracy in a fast and non-destructive way. By measuring the capacitance transient, the technique is uniquely able to distinguish between mobile cations and anions, with concentrations as low as 0.01% of the doping density.

Transient ion-drift measures the change of capacitance over time under a constant bias. Assuming thermal diffusion to be negligible against drift and that the total ion concentration is conserved, the ion diffusion equation is given by:

$$\frac{\delta N_{ion}}{\delta t} = \frac{\delta(N_{ion}\mu E)}{\delta x}$$

where μ is the ion mobility and E is the electric field. Assuming that the electric field varies linearly across the depletion region, the electric field can be written as $E(x) = E_0(1 - \frac{x}{W_D})$, where W_D is the depletion width.[12] Assuming that the ions are initially uniformly distributed, the capacitance transient induced by ion drift is given by:

$$N_{ion}(t) = N_{ion0} \exp\frac{t}{\tau}$$

where N_{ion0} is the initial ion concentration and $\tau = \frac{W_D}{\mu E_M}$. Using the Einstein relation ($\mu = \frac{D\,q}{k_B T}$) and expressing the electric field as a function of the doping density N as $E_0 = \frac{q\,W_D N}{\varepsilon_0\,\varepsilon}$, where q is the elementary charge, ε_0 is the vacuum permittivity, and ε is the perovskite permittivity, the time constant can be written as:

$$\tau = \frac{k_B\,T\,\varepsilon_0\,\varepsilon}{q^2 D\,N}$$

where k_B is the Boltzmann constant and T the temperature. $D = \frac{\nu_0 d^2}{6} e^{-\frac{E_A}{k_B T}}$ is the ion diffusion-coefficient where ν_0 is the attempt-to-escape frequency of an ionic jump, d the jump distance, and E_A the activation energy.[13]

To quantify ion migration within the perovskite layer, one has to carefully chose a perovskite device structure to avoid capacitive hysteresis, interfacial effects, and ion migration within the transport layers (see also section S1). It is not possible to distinguish between mobile ions within the perovskite layer and mobile ions within the other layers of the device structure. It is thus important to avoid, as far as possible, mobile ions within the other layers of the device structure. For measuring capacitance transients, one furthermore has to carefully chose an AC measurement frequency to measure the capacitance change of the perovskite layer. Most commercially available capacitance transient measurement systems use a fixed AC measurement frequency of 1 MHz. Measuring capacitance transients with such a high frequency requires devices with a very low series resistance. For most perovskite-based devices, however, the series resistance of the transparent conductive oxide starts to dominate the impedance response at such high frequencies (see also section S6). We thus conclude that an AC measurement frequency of 1 MHz is not suitable for measuring capacitance transients of perovskite devices in the majority of cases.

S6 FITTING CAPACITANCE TRANSIENTS

Figure S7 shows measured capacitance transients from 180 to 350 K with steps of 10 K measured at 0 V after applying a voltage pulse of 0.4 V for 1 second (identical to Figure 3a of the main text). The grey dotted lines in Figure S7(a) indicate the modelled capacitance decay due to ionic drift according to the values in Table S1. For the Arrhenius plot we limited the data analysis to temperatures where the number of exponentials to use was evident from the scan and the fit quality was good (as indicated by the colors in Figure 3c of the main text). Figure S7(b) to (e) exemplary show fits to capacitance decays at 200, 240, 290, and 340 K.

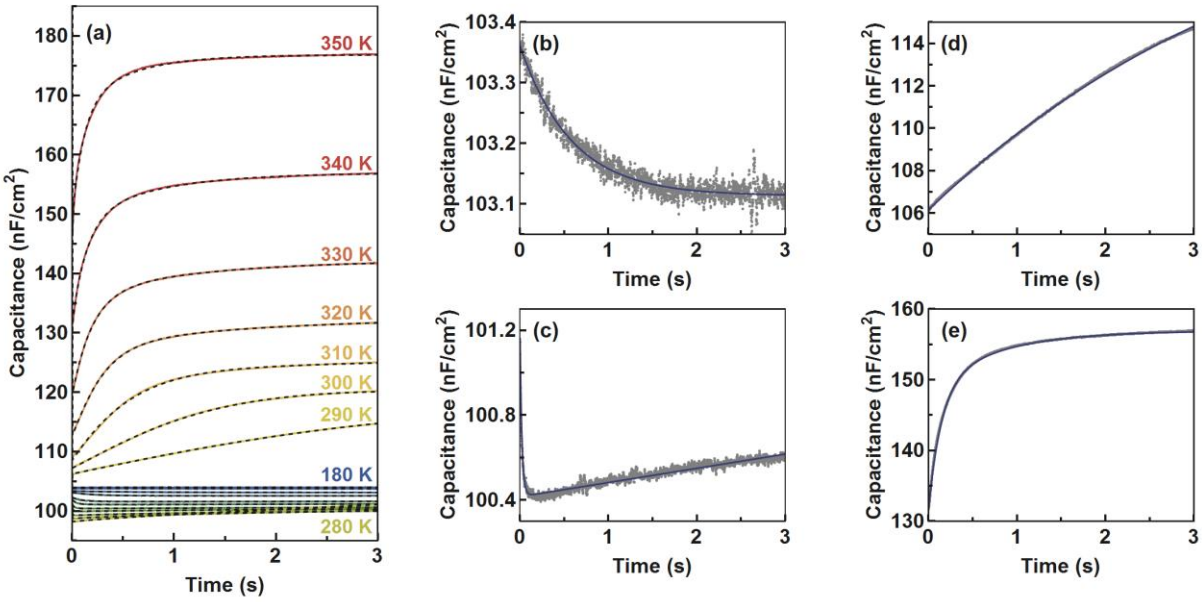

Figure S7. (a) Measured capacitance transients together with the modelled capacitance decay due to ionic drift of A1, C1, and C2 shown as black dotted lines. Exemplary fits of measured capacitance decay at 200 **(b)**, 240 **(c)**, 290 **(d)**, and 340 K **(d)**. One exponential decay function is used to fit (b) and (d) and two exponential decay functions to fit **(c)** and **(e)**. Grey points are experimentally measured data and blue lines are obtained fits.

S7 IMPEDANCE SPECTROSCOPY

In a perovskite solar cell, mobile ions can migrate through the transport layer towards the electrodes. [14] As metals are prone to reacting with I^- ion, this ion migration can induce an additional series resistance related to contact degradation.[15] It is thus important to carefully choose an AC measuring frequency for which the impedance response corresponds to the capacitive character of the device, as oppose to the resistances.

Figure S8 shows the impedance response of the perovskite solar cells at different temperatures. A phase angle close to −90° indicate that the impedance corresponds to the capacitance of the device. At frequencies above 10 kHz, the phase angle increases while the modulus approaches the series resistance of the device, indicating that the capacitance response is governed by the series resistance. We therefore measure the capacitance as a

function of voltage and time with an AC frequency of 10 kHz, where the impedance response is dominated by the capacitance of the device over the whole temperature range of interest.

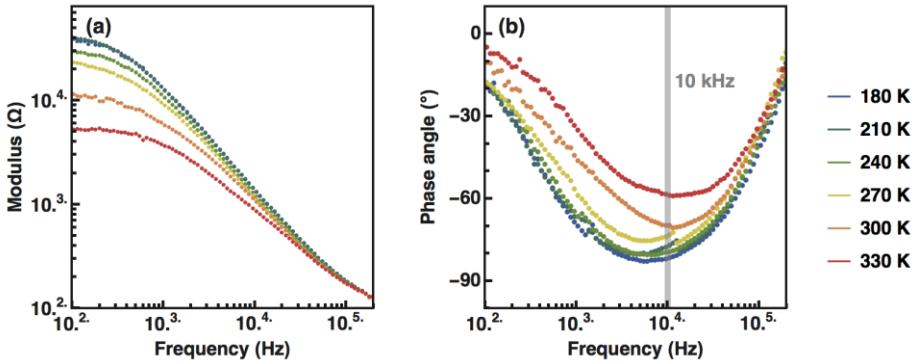

Figure S8. Impedance spectroscopy of an inverted perovskite solar cell (NiO_x/$MAPbI_3$/C_{60}) measured at 0 V with an AC perturbation of 20 mV in the dark, separated in **(a)** modulus and **(b)** phase angle.

S8 TRANSIENT ION-DRIFT VERSUS DEEP-LEVEL TRANSIENT SPECTROSCOPY

To distinguish between ion diffusion and electronic effects such as trapping and de-trapping, we compare the rise and decay time of capacitance following the forward bias and returning to short circuit conditions.[12] For mobile ions, it is expected that the time required to lead to a uniform ion distribution after applying a forward bias is longer than the time required for ions to drift back to the interfaces after removal of the forward bias. In contrast, for traps the capture rate is much higher than the emission rate. Figure S9 shows the measured capacitance transient of an inverted perovskite solar cell measured at 210 K, showing that the measured capacitive transient is due to the diffusion of mobile ions.

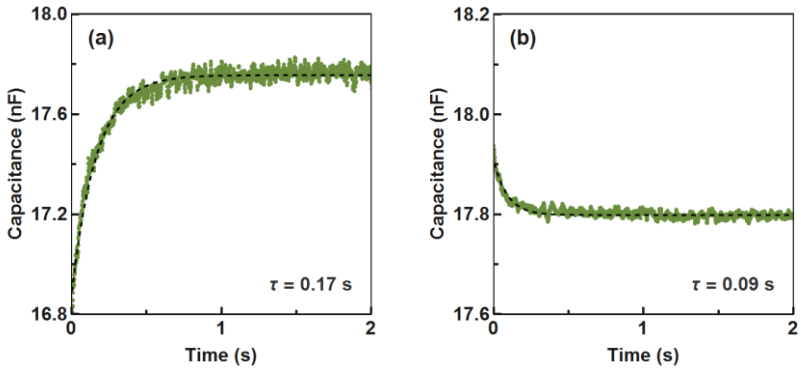

Figure S9. Capacitance transient of an inverted perovskite solar cell (NiO_x/$MAPbI_3$/C_{60}) measured in the dark **(a)** while applying a voltage pule of 0.4 V and **(b)** at short circuit, after removing the voltage bias. The dashed lines are fits obtained using an exponential decay function with the timescale indicated in the inset.

S9 STATISTICS AND REPRODUCIBILITY ACROSS LABORATORIES

Many examples in the literature show that the performance of perovskite solar cells depend heavily on the fabrication, even in the same laboratory. Also, ions are presumably affected by, and affecting degradation. To study this, we measure seven different devices and compare the transient ion-drift response.

Device #1 corresponds to the device shown in Figure 1 and Figure 3 the main text. Device #2 corresponds to a device fabricated in the same way as device #1. Device #3 represent a poor performing device. Devices #4, #5, and #6 are devices fabricated in the laboratory of the University of Konstanz. All devices have the same device structure (NiO_x/$MAPbI_3$/C_{60}), but the $MAPbI_3$ layer has an average thickness of 105 nm in devices #1, #2 and #3 and 275 nm in devices #4, #5 and #6. The values obtained for activation energy, diffusion coefficient, and concentration for mobile ions for the measured samples are summarized in Table S1 – S6. Note that we could not resolve the slow MA^+ species in the devices manufactured at the University of Konstanz.

A typical current-voltage characteristic curve together with an external quantum efficiency spectrum of an inverted perovskite solar cell fabricated in Konstanz is shown in Figure S10.

We furthermore note that in devices with an average $MAPbI_3$ thickness of 275 nm, we observed an initial capacitance decay at high temperatures related to the redistribution of ions inside the depletion layer (see Figure S11).[16] For DLTS, such an initial decay in capacitance is not expected, as the drift of free charge carriers out of the depletion layer is much faster than the emission rate. The capacitance change due to transient ion-drift, however, can be due to a combination of both the redistribution inside the depletion layer and the drift of mobile ions towards the contacts.

Table S1. Characteristics of mobile ions in device #1 with a short-circuit current density of 17.7 mA/cm^2, an open-circuit voltage of 0.98 V, a fill factor of 56%, and a power-conversion efficiency of 9.6%.

	A1	C1		C2
Migrating ion species	I^-	MA^+		MA^+
Charge	negative	positive		positive
Concentration (cm^{-3})	$(1.7 \pm 0.1) \times 10^{15}$	$(2.5 \pm 0.1) \times 10^{16}$		$(1.1 \pm 0.1) \times 10^{16}$
Phase structure	tetragonal	tetragonal	cubic	cubic
Activation energy (eV)	0.37 ± 0.01	0.95 ± 0.02	0.28 ± 0.01	0.43 ± 0.01
Diffusion coefficient at 300 K (cm^2 s^{-1})	$(3.2 \pm 1.4) \times 10^{-9}$	$(1.8 \pm 2.4) \times 10^{-12}$	$(4.7 \pm 2.7) \times 10^{-12}$	$(4.4 \pm 3.7) \times 10^{-13}$

Table S2. Characteristics of mobile ions in device #2 with a short-circuit current density of 13.4 mA/cm^2, an open-circuit voltage of 0.88 V, a fill factor of 48%, and a power-conversion efficiency of 5.7%.

	A1	C1		C2
Migrating ion species	I^-	MA^+		MA^+
Charge	negative	positive		positive
Concentration (cm^{-3})	$(2.1 \pm 0.1) \times 10^{15}$	$(3.9 \pm 0.1) \times 10^{15}$		$(2.4 \pm 0.1) \times 10^{15}$
Phase structure	tetragonal	tetragonal	cubic	cubic
Activation energy (eV)	0.39 ± 0.01	0.40 ± 0.01	0.23 ± 0.02	0.04 ± 0.03
Diffusion coefficient at 300 K (cm^2 s^{-1})	$(11.6 \pm 2.5) \times 10^{-9}$	$(3.4 \pm 2.1) \times 10^{-12}$	$(6.4 \pm 11.1) \times 10^{-12}$	$(1.6 \pm 3.7) \times 10^{-12}$

Table S3. Characteristics of mobile ions in device #3 with a short-circuit current density of 3.6 mA/cm^2, an open-circuit voltage of 0.74 V, a fill factor of 37%, and a power-conversion efficiency of 1.0%.

	A1	C1		C2
Migrating ion species	I^-	MA^+		MA^+
Charge	negative	positive		positive
Concentration (cm^{-3})	$(2.1 \pm 0.1) \times 10^{15}$	$(3.4 \pm 0.1) \times 10^{15}$		$(1.7 \pm 0.1) \times 10^{15}$
Phase structure	tetragonal	tetragonal	cubic	cubic
Activation energy (eV)	0.23 ± 0.01	0.26 ± 0.01	0.62 ± 0.01	0.71 ± 0.01
Diffusion coefficient at 300 K (cm^2 s^{-1})	$(2.2 \pm 0.8) \times 10^{-9}$	$(11.5 \pm 2.1) \times 10^{-12}$	$(20.1 \pm 16.6) \times 10^{-12}$	$(2.8 \pm 2.7) \times 10^{-12}$

Table S4. Characteristics of mobile ions in device #5 with a short-circuit current density of 14.9 mA/cm^2, an open-circuit voltage of 0.96 V, a fill factor of 62%, and a power-conversion efficiency of 8.8%.

	A1	C1	
Migrating ion species	I^-	MA^+	
Charge	negative	positive	
Concentration (cm^{-3})	$(4.3 \pm 0.3) \times 10^{12}$	$(1.6 \pm 0.1) \times 10^{16}$	
Phase structure	tetragonal	tetragonal	cubic
Activation energy (eV)	0.28 ± 0.09	1.91 ± 0.06	0.94 ± 0.06
Diffusion coefficient at 300 K (cm^2 s^{-1})	$(0.2 \pm 1.8) \times 10^{-9}$	$(5.3 \pm 23.2) \times 10^{-15}$	$(1.7 \pm 7.1) \times 10^{-13}$

Table S5. Characteristics of mobile ions in device #6 with a short-circuit current density of 16.1 mA/cm^2, an open-circuit voltage of 0.97 V, a fill factor of 66%, and a power-conversion efficiency of 10.2%.

	A1	C1	
Migrating ion species	I^-	MA^+	
Charge	negative	positive	
Concentration (cm^{-3})	$(7.0 \pm 1.4) \times 10^{13}$	$(1.8 \pm 0.2) \times 10^{16}$	
Phase structure	tetragonal	tetragonal	cubic
Activation energy (eV)	0.16 ± 0.05	0.96 ± 0.07	0.25 ± 0.03
Diffusion coefficient at 300 K (cm^2 s^{-1})	$(0.06 \pm 0.26) \times 10^{-9}$	$(2.0 \pm 11.3) \times 10^{-13}$	$(2.5 \pm 5.9) \times 10^{-12}$

Table S6. Characteristics of mobile ions in device #7 with a short-circuit current density of 17.2 mA/cm^2, an open-circuit voltage of 1.02 V, a fill factor of 70%, and a power-conversion efficiency of 12.1%.

	A1
Migrating ion species	I^-
Charge	negative
Concentration (cm^{-3})	(6.9 ± 0.8) x 10^{14}
Phase structure	tetragonal
Activation energy (eV)	0.32 ± 0.05
Diffusion coefficient at 300 K (cm^2 s^{-1})	(1.2 ± 5.7) x 10^{-9}

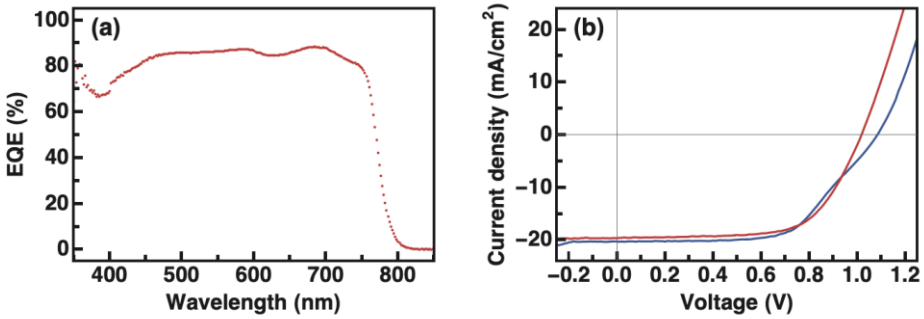

Figure S10. (a) Current-voltage characteristic curve and **(b)** external quantum efficiency (EQE) spectrum of an inverted perovskite solar cell fabricated in Konstanz with a short-circuit current density of 19.9 mA/cm^2, an open-circuit voltage of 1.04 V, a fill factor of 63%, and a power-conversion efficiency of 13.0%. The integrated current density of the EQE spectrum with the AM1.5G solar spectrum is 21.1 mA/cm^2, very close to the value obtained from the current-voltage measurements.

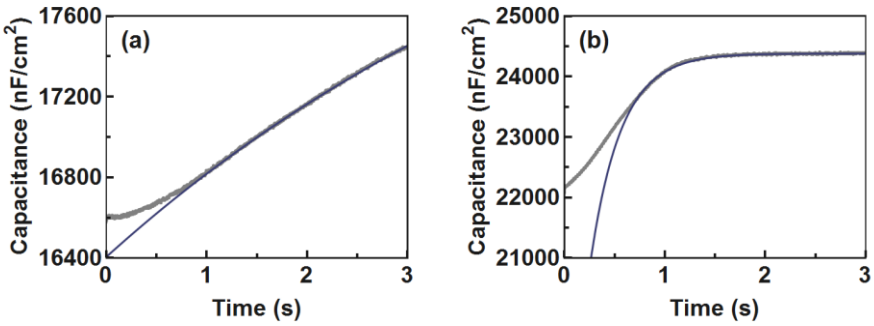

Figure S11. Ion-drift-induced capacitance transient measured at **(a)** 320 and at **(b)** 340 K in addition to an initial capacitance decrease related to the redistribution of ions inside the depletion layer.[16] Grey points are experimentally measured data and blue lines are single exponential fits.

S10 EXPERIMENTAL METHODS

Device fabrication. Device #1, device #2, and #3 were fabricated as described hereafter, with the exception of device #2 which was fabricated using a NiO_x precursor solution of 0.3M that was spun on the cleaned ITO glass at 4000 rpm for 15 seconds: The $MAPbI_3$ perovskite precursor solution was prepared by mixing of total 1.5 M of methylammonium iodide (MAI, Solaronix) and lead(II) iodide (PbI_2, TCI) with 1:1 molar ratio dissolved in N, N-dimethylformamide (anhydrous, Aldrich) and DMSO for 3 hours at 60 °C. 50 µL of the MAPbI3 precursor solution filtered through a 0.45 µm sized PTFE membrane was spun onto NiO_x coated substrates at 4000 rpm for 50 seconds in a nitrogen-filled glove box. 10 seconds after the beginning of the rotation, 300 µL of Diethyl ether anti-solvent (anhydrous, Aldrich) was quickly dropped onto the substrate. After the $MAPbI_3$ spinning process, the substrates were annealed at 100 °C for 3 minutes. 45 nm of C60 (0.2 Å/s rate) was deposited on top of the $MAPbI_3$ layer by thermal sublimation at pressures below 8×10^{-6} mbar. A thin layer of bathocuproine (99.99%, Aldrich) dissolved in ethanol (0.5 mg/ml) was then spun on top of the C_{60} layer with 6000 rpm for 15 seconds. Finally, 100 nm of silver (1 Å/s) was deposited by thermal evaporation at pressures below 8×10^{-6} mbar.

Device #4, device #5, and #6 were fabricated as described hereafter: Laser patterned indium tin oxide (ITO) glass substrates were cleaned by ultra-sonication for 20 minutes subsequently in detergent in deionized water, deionized water, acetone, and isopropanol, followed by oxygen plasma for 20 minutes at 100 W. Nickel oxide (NiO_x) precursor solution (0.1 M nickel(II) nitrate hexahydrate (Aldrich) in ethanol) filtered with a 0.45 µm PTFE membrane was spun on the cleaned ITO glass at 4000 rpm for 30 seconds. This step was then repeated two times.[14] Annealing at 350 °C for 1 hour with a ramping speed of 3 °C/min induced NiO_x film formation. The $MAPbI_3$ perovskite precursor solution was prepared by mixing of total 1.35 M of methylammonium iodide (MAI, solaronix) and lead(II) iodide (PbI_2, Aldrich) with 1:1 molar ratio dissolved in N,N-dimethylformamide (anhydrous, Aldrich) at 60 °C. The $MAPbI_3$ precursor solution was filtered through a 0.45 µm PTFE membrane spun onto NiO_x coated substrates at 5000 rpm for 25 seconds in a nitrogen filled glove box. 5 seconds after the beginning of the rotation, 180 µL of chlorobenzene anti-solvent (anhydrous, Aldrich) was quickly dropped onto the substrate. After the $MAPbI_3$ spinning process, the substrates were annealed at 100 °C for 15 minutes. 30 nm of C_{60} (0.5 Å/s rate, 99.9%, Aldrich), 8 nm of bathocuproine (0.2 Å/s, 99.99%, Aldrich), 50 nm of silver (1 Å/s, 99.99%, Kurt J. Lesker) and 150 nm of gold electrode (1 Å/s, 99.999%, Kurt J. Lesker) were sequentially deposited on top of $MAPbI_3$ layer by thermal sublimation/evaporation at pressures below 2×10^{-7} mbar.

Electrical measurements. To avoid air exposure, the sample was loaded into a Janis VPF-100 liquid nitrogen cryostat inside a nitrogen-filled glovebox. Current-voltage, impedance spectroscopy, capacitance-voltage, and transient ion-drift measurements were performed at a pressure below 2×10^{-6} mbar in the dark using a commercially available DLTS system from Semetrol. To ensure thermal equilibrium the temperature of the sample was held constant for

at least 30 minutes before current-voltage, impedance spectroscopy, and capacitance-voltage measurements. The capacitance was modelled by a capacitor in parallel with a conductance. Capacitance transient measurements were performed from 180 to 350 K in steps of 2 K with a heating rate of about 2 K per minute. The sample was held at 180 K for one hour before starting the transient ion-drift measurement.

Imaging of device cross-section. To obtain a clean cross-section of the device, it was immersed in liquid nitrogen for 60 seconds and cleaved in the center. The cross-sectional image was taken with a FEI Verios 460 scanning electron microscope in the secondary electron mode. An acceleration voltage of 5 kV and a working distance of 4 mm were used and field immersion mode was applied for an optimized resolution.

References

(1) Garcia-Belmonte, G.; Bisquert, J. Distinction between Capacitive and Noncapacitive Hysteretic Currents in Operation and Degradation of Perovskite Solar Cells. *ACS Energy Letters*. American Chemical Society October 14, 2016, pp 683–688. https://doi.org/10.1021/acsenergylett.6b00293.

(2) Deng, L. L.; Xie, S. Y.; Gao, F. Fullerene-Based Materials for Photovoltaic Applications: Toward Efficient, Hysteresis-Free, and Stable Perovskite Solar Cells. *Advanced Electronic Materials*. December 5, 2017, p 1700435. https://doi.org/10.1002/aelm.201700435.

(3) Kim, H.-S.; Jang, I.-H.; Ahn, N.; Choi, M.; Guerrero, A.; Bisquert, J.; Park, N.-G. Control of I-V Hysteresis in CH3NH3PbI3 Perovskite Solar Cell. *J. Phys. Chem. Lett.* **2015**, *6* (22), 4633–4639. https://doi.org/10.1021/acs.jpclett.5b02273.

(4) Zhu, Z.; Bai, Y.; Zhang, T.; Liu, Z.; Long, X.; Wei, Z.; Wang, Z.; Zhang, L.; Wang, J.; Yan, F.; et al. High-Performance Hole-Extraction Layer of Sol-Gel-Processed NiO Nanocrystals for Inverted Planar Perovskite Solar Cells. *Angew. Chemie - Int. Ed.* **2014**, *53* (46), 12571–12575. https://doi.org/10.1002/anie.201405176.

(5) Chen, W.; Wu, Y.; Yue, Y.; Liu, J.; Zhang, W.; Yang, X.; Chen, H.; Bi, E.; Ashraful, I.; Grätzel, M.; et al. Efficient and Stable Large-Area Perovskite Solar Cells with Inorganic Charge Extraction Layers. *Science* **2015**, *350* (6263), 944–948. https://doi.org/10.1126/science.aad1015.

(6) Mosconi, E.; Meggiolaro, D.; Snaith, H. J.; Stranks, S. D.; De Angelis, F. Light-Induced Annihilation of Frenkel Defects in Organo-Lead Halide Perovskites. *Energy Environ. Sci.* **2016**, *9* (10), 3180–3187. https://doi.org/10.1039/C6EE01504B.

(7) DeQuilettes, D. W.; Zhang, W.; Burlakov, V. M.; Graham, D. J.; Leijtens, T.; Osherov, A.; Bulović, V.; Snaith, H. J.; Ginger, D. S.; Stranks, S. D. Photo-Induced Halide Redistribution in Organic-Inorganic Perovskite Films. *Nat. Commun.* **2016**, *7*, 11683. https://doi.org/10.1038/ncomms11683.
(8) Brivio, F.; Butler, K. T.; Walsh, A.; van Schilfgaarde, M. Relativistic Quasiparticle Self-Consistent Electronic Structure of Hybrid Halide Perovskite Photovoltaic Absorbers. *Phys. Rev. B* **2014**, *89* (15).
(9) Sze. *Physics of Semiconductor Devices*; Wiley-Interscience, 2014; Vol. 10. https://doi.org/10.1007/978-3-319-03002-9.
(10) Frolova, L. A.; Dremova, N. N.; Troshin, P. A. The Chemical Origin of the P-Type and n-Type Doping Effects in the Hybrid Methylammonium-Lead Iodide (MAPbI3) Perovskite Solar Cells. *Chem. Commun.* **2015**, *51* (80), 14917–14920. https://doi.org/10.1039/c5cc05205j.
(11) Almora, O.; Aranda, C.; Mas-Marzá, E.; Garcia-Belmonte, G. On Mott-Schottky Analysis Interpretation of Capacitance Measurements in Organometal Perovskite Solar Cells. *Appl. Phys. Lett.* **2016**, *109* (17), 173903. https://doi.org/10.1063/1.4966127.
(12) Heiser, T.; Mesli, A. Determination of the Copper Diffusion Coefficient in Silicon from Transient Ion-Drift. *Appl. Phys. A Solids Surfaces* **1993**, *57* (4), 325–328. https://doi.org/10.1007/BF00332285.
(13) Meggiolaro, D.; Mosconi, E.; De Angelis, F. Formation of Surface Defects Dominates Ion Migration in Lead-Halide Perovskites. *ACS Energy Lett.* **2019**, *4* (3), acsenergylett.9b00247. https://doi.org/10.1021/acsenergylett.9b00247.
(14) Yin, X.; Yao, Z.; Luo, Q.; Dai, X.; Zhou, Y.; Zhang, Y.; Zhou, Y.; Luo, S.; Li, J.; Wang, N.; et al. High Efficiency Inverted Planar Perovskite Solar Cells with Solution-Processed NiOx Hole Contact. *ACS Appl. Mater. Interfaces* **2017**, *9* (3), 2439–2448. https://doi.org/10.1021/acsami.6b13372.
(15) Guerrero, A.; You, J.; Aranda, C.; Kang, Y. S.; Garcia-Belmonte, G.; Zhou, H.; Bisquert, J.; Yang, Y. Interfacial Degradation of Planar Lead Halide Perovskite Solar Cells. *ACS Nano* **2016**, *10*, 218–224. https://doi.org/10.1021/acsnano.5b03687.
(16) Heiser, T.; Weber, E. Transient Ion-Drift-Induced Capacitance Signals in Semiconductors. *Phys. Rev. B* **1998**, *58* (7), 3893–3903. https://doi.org/10.1103/PhysRevB.58.3893.